ACS APPLIED MATERIALS & INTERFACES

www.acsami.org

Research Article

Residual Compressive Stress Enabled 2D-to-3D Junction Transformation in Amorphous Carbon Films for Stretchable Strain Sensors

Xin Ma, Qi Zhang,* Peng Guo,* Xiaoshan Tong, Yulong Zhao,* and Aiying Wang*

Cite This: *ACS Appl. Mater. Interfaces* 2020, 12, 45549−45557

Read Online

ACCESS | Metrics & More | Article Recommendations | Supporting Information

ABSTRACT: Usually, two-dimensional (2D) flexible strain sensors based on cracks have very high sensitivities but small measuring ranges, while the three-dimensional (3D) ones behave in the opposite way. Here, by utilizing the large residual compressive stress of an amorphous carbon (a-C) film and the flexibility of polydimethylsiloxane (PDMS), we developed a facile and economic strategy to fabricate a high-sensitive a-C/PDMS stretchable strain sensor. Results showed that for the first time, the a-C film ranging from 25 nm to 1 μm changed the shape and orientation of conductive scales, as well as made a one-step 2D-to-3D electrical junction transformation in integrated sensors. In particular, the sensor with a 1 μm thick a-C film exhibited the best comprehensive performance, displaying a maximum gauge factor of 746.7 and strain range up to 0.5. However, the linearity decreased slightly as the strain range went beyond 0.43. Additionally, the sensor showed a satisfactory repeatability for 5000 cycles, together with excellent time and temperature drift performances at zero position of 75 ppm full scale (FS) and 25 ppm FS·°C^{-1} in the range of −20 to 155 °C, respectively. The sensor has large potentials for wearable devices used in the monitoring of various human motions and physiological signals.

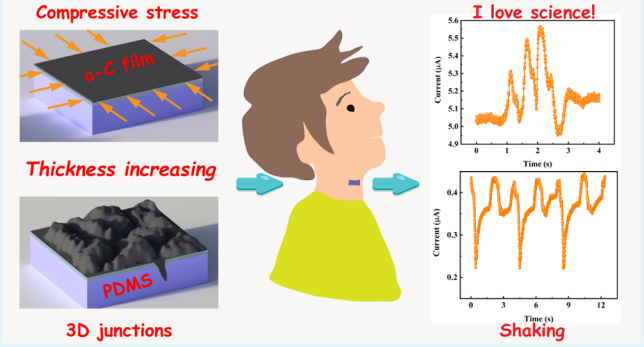

KEYWORDS: *amorphous carbon film, stretchable strain sensors, compressive stress, 2D−3D junction transformation, microstructure*

1. INTRODUCTION

A stretchable strain sensor is a core component of wearable devices, soft robots, and health-monitoring devices.[1−3] Usually, the strain change is detected through piezoresistive, capacitive, and piezoelectric sensing characteristics.[4] In particular, the piezoresistive sensor is widely used in strain sensing owing to the convenient transformation of the strain variation into electrical signal.[5−8] Recently, increasing progress has been achieved in the development of crack-based flexible strain sensors, where the ultrahigh sensitivities mainly originate from the unstable electrical connections between adjacent conductive scales. For example, Song et al. have reported a compressive strain sensor based on carbon black cracks with a gauge factor (GF) of 647,[9] while an ultrasensitive strain sensor based on graphene armor scales with a GF of up to 1054 was reported by Yang et al.[10] Using micromachining process to fabricate cracks, a higher GF of even over 5888 was even achieved.

For these crack-based flexible strain sensors, the electrical conduction mechanisms can be roughly divided into two-dimensional (2D) and three-dimensional (3D) contact modes. In the 2D mode, the conductive scales are covered with conductive films (with a thickness of several hundred nanometers or slightly larger) and contact with each other in one plane, which greatly limited the contact area. Therefore, the strain sensitivity is usually very high, but only a small strain can be detected, in view of the two following facts. First, with increasing applied strain, the resistance of the crack-based sensors can increase quickly, to exceed the upper limit of the electric meter. In addition, the linear ranges of these sensors are usually quite small, which will also limit their application.[11−14] Conversely, in the 3D mode, conductive scales or blocks constitute electrical loops through face or solid contacts. Their resistivities and sensitivities are usually smaller so that they can easily detect larger strains. In addition, the output signals are smoother and more stable due to the higher contact performances between adjacent conductive cells. This is important for the development of a high-performance strain sensor. However, the fabrication of the 3D-mode sensors are usually complex[15−17] and require longer process times than those for the 2D-mode sensors.

Received: July 3, 2020
Accepted: September 9, 2020
Published: September 9, 2020

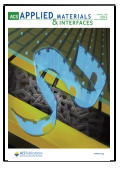

https://dx.doi.org/10.1021/acsami.0c12073
ACS Appl. Mater. Interfaces 2020, 12, 45549−45557

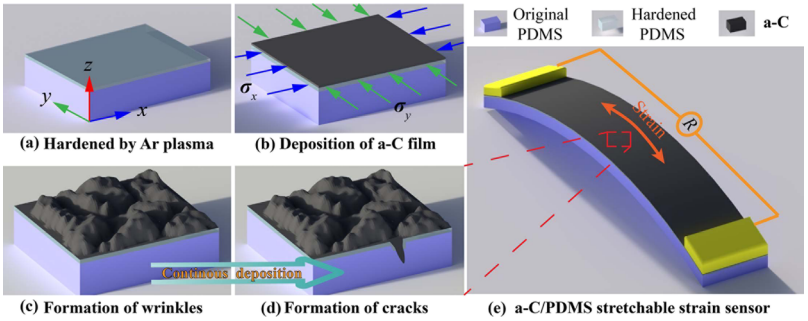

Figure 1. Schematic of the 2D-to-3D transformation mechanism of the fabricated a-C/PDMS sensor, (a) hardening and cleaning of the PDMS substrate by Ar plasma, (b) a-C film coated on the hardened PDMS substrate and the corresponding residual compressive stress with thickness, (c) relaxation of the large residual stress enabled the formation of wrinkles, (d) formation of original cracks (3D junctions) due to the bending and fracture of the multilayer structure, and (e) illustration of the a-C/PDMS sensor.

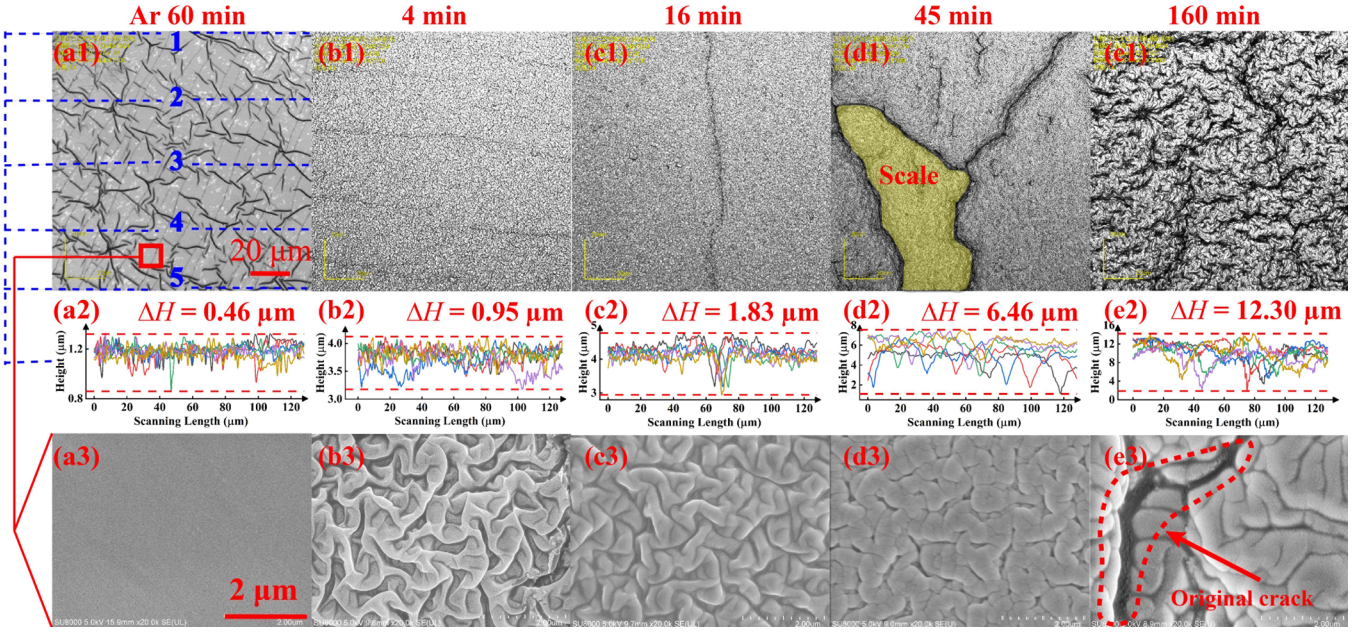

Figure 2. (a–e) Ar plasma-hardened PDMS substrate, hardened PDMS with 4, 16, 45, and 160 min a-C film, showing the obviously changed morphologies. (Series 1) confocal microscopy images of the morphologies in which the valleys appear. (Series 2) height profiles along the lines 1–5, showing the increased depth of original valleys. (Series 3) SEM images of the microstructures, showing similar wrinkles and the original crack in the 160 min sample.

Extensive studies have been carried out to combine the advantages of 2D and 3D modes by utilizing the differences in adhesion force and elasticity modulus of multilayer systems (e.g., Cr, polyimide (PI), SU8, polydimethylsiloxane (PDMS), vinyl polysiloxane, etc.). By coupling with auxiliary extra-operations such as prestretching, compression, or thermal contraction, the 2D multilayer groups can be transformed into 3D microstructures.[18−21] As a result, a high-performance crack-based flexible strain sensor can be fabricated by modifying the electrical junctions between the scales, for example, by bending the edges of the scale in a microlevel to obtain a larger contact area.[22] However, if one keeps in mind the technology complexity and controllable stability, to develop a facile technique based on thin films for a high-performance sensor is still an open challenge.

In this study, we proposed a simple method to prepare high-performance sensors with both the advantages of 2D and 3D modes; here, an amorphous carbon (a-C) film was used as a functional film owing to its high piezoresistive gauge factor and very large residual stress up to 3 GPa.[23,24] The soft and stretchable PDMS was selected as a substrate, and the high-performance stretchable a-C/PDMS sensors were designed and fabricated. Taking into account the excellent adhesion strength between the a-C film and the substrate observed in our previous results, it is expected that the deposited film will not be peeled off under such big stress in the present case.[25] Using a high compressive stress, a one-step 2D-to-3D electrical junction transformation in a-C films was first presented. The sensing behavior was studied by adjusting the thickness of the a-C film, and the sensitivity, stability, repeatability, and time/temperature drift performance of the fabricated sensors were evaluated. Additionally, a test for monitoring of human motions and physiological signals of the neck during speaking, swallowing, head nodding, rising, and shaking, and heart beating showed the excellent performance of the sensor in real applications. The electrical conduction mechanism during the 2D-to-3D transformation process was discussed in terms of the evolution of the combined structures in a-C/PDMS.

https://dx.doi.org/10.1021/acsami.0c12073
ACS Appl. Mater. Interfaces 2020, 12, 45549−45557

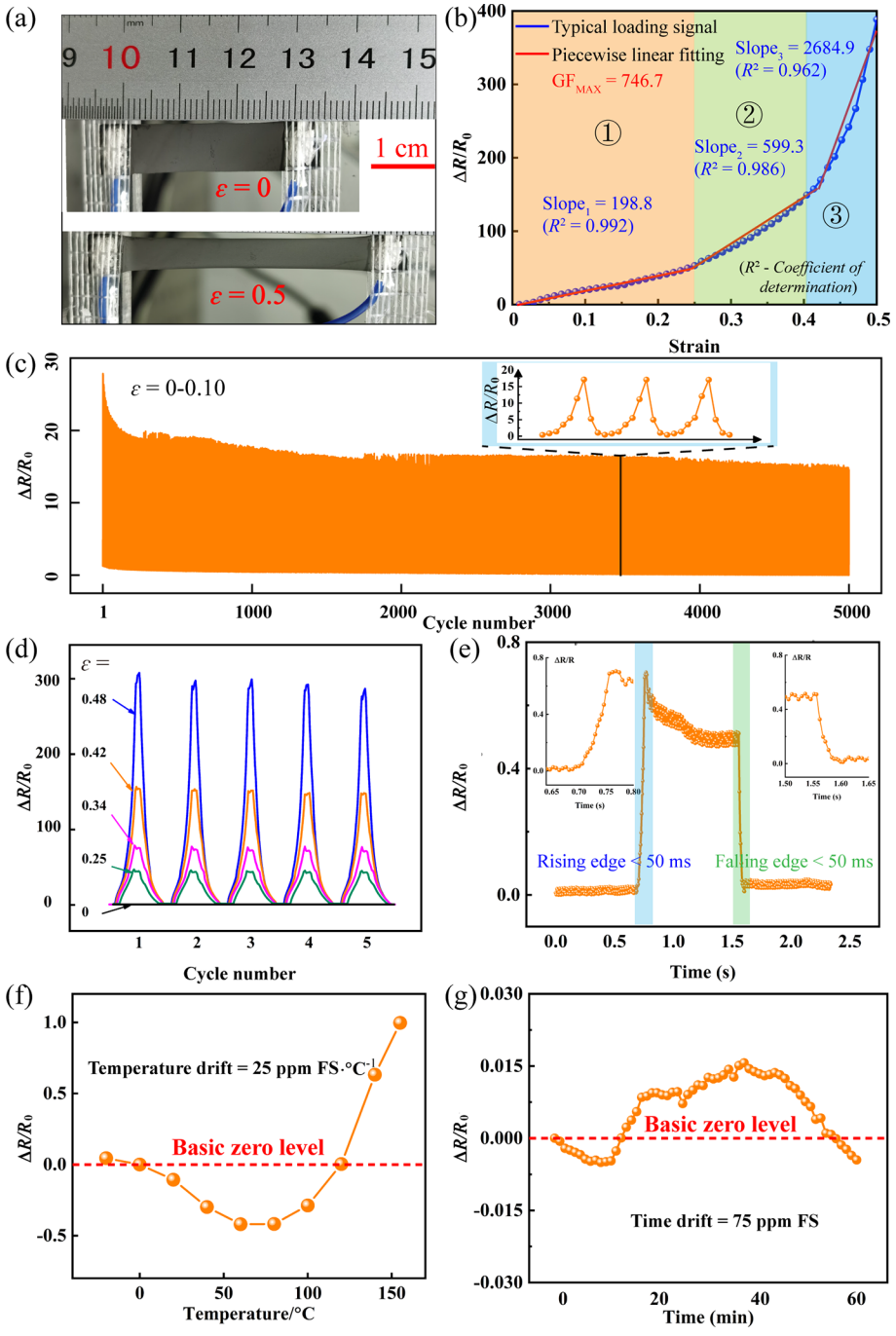

Figure 3. Electrical performance test results. (a) Images of the sensor under testing (ε = 0 and 0.5), (b) GF test result for the 160 min sample and piecewise linear fitting, showing good linearity in the first two stages, (c) repeatability test results (5000 cycles) for the 160 min sample and the inset showing the magnified view of typical three cycles, (d) test result (five cycles) for the 160 min sample at various strains, showing good repeatability under different strains, (e) response time evaluation of the 160 min sample (detailed views of the rising and falling parts are shown in the insets), and (f, g) good temperature and time drift performances of the 160 min sample at zero position, respectively.

2. EXPERIMENTAL SECTION

2.1. Deposition of a-C Film. The a-C films (one of the hydrogen-free amorphous carbon films) were deposited using a direct-current (DC) magnetron sputtering system (Figure S1). It is noted that the reason for selecting the a-C films is due to the variety of amorphous carbon films and complexity in atomic carbon bonds. Before deposition, a thickness of 200 μm PDMS was fabricated as the substrate and fixed on a rotated substrate holder in a deposition vacuum chamber. More details about the film deposition technique can be referred from our previous work.[26] To obtain a higher adhesion strength, the PDMS substrate was first etched by Ar^+ plasma for 60 min at a pulsed substrate bias voltage of −450 V and the working pressure was 1.1 Pa, which also hardened the PDMS surface.[27] During the subsequent a-C deposition, Ar gas (a flow rate of 65 sccm) was introduced into the chamber and ignited the sputtering of the graphite target with a working pressure of 0.3 Pa and a DC power at 2.1 kW. Moreover, the substrate was rotated at a speed of 10 rpm during the deposition to enhance the film uniformity. The deposition time was controlled (4, 16, 45, and 160 min) to study the effect of the thickness on the evolution of the microstructure, where the corresponding thicknesses were approximately 25, 100, 300 nm, and 1 μm, respectively.

https://dx.doi.org/10.1021/acsami.0c12073
ACS Appl. Mater. Interfaces 2020, 12, 45549−45557

2.2. Fabrication of the PDMS Substrate and the Sensor. The PDMS substrate was fabricated using the following process. First, a prepolymer and a curing agent (Sylgard 184, Dow Corning) were mixed in a weight ratio of 10:1. Liquid PDMS was then spin-coated on a 4-inch silicon substrate to a thickness of approximately 200 μm. After baking at 120 °C for 30 min, the PDMS membrane was carefully peeled off from the silicon substrate. After deposition, the PDMS coated with a-C films in a range of thickness was cut into rectangle specimens, with dimensions of 40/12 mm × 10 mm × 200 μm (length × width × thickness). The effective length was about 28/8 mm. The Al wires were connected to the sensors using a conductive silver paste, which was solidified at 120 °C for 20 min. In the human motion and physiological signal tests, the sensor was pasted onto the skin using the commercial double-sticky tape.

2.3. Characterization Method. The morphologies of the original surface and fabricated wrinkles/cracks were comprehensively monitored by scanning electron microscopy (SEM, SU8010, Hitachi), confocal microscopy (OLS4000, Olympus), and atomic force microscopy (Innova, Bruker). X-ray photoelectron spectroscopy (XPS, Axis Ultra DLD) was used to analyze the phase content of the a-C films. The thickness of the deposited a-C film was evaluated using a profilometer (Alpha-Step IQ) on a silicon substrate. Using the Stoney equation and a laser tester (JLCST022, J&L Tech Co. Ltd.), the residual stress of the a-C film was calculated based on the curvature of the a-C-coated 100 μm thick silicon substrate, and the ratio of length/width was beyond 10. The Young's modulus of the a-C film was evaluated by nanoindentation in a Continuous Contact Module (G200, MTS) with the maximum indentation depth at 150 nm. A single-column testing machine (ESM303, Mark-10) was used to test the mechanical performance of the sensor. The sheet resistance was tested using a four-point probe resistance tester (GP1599, Kaivo). In the testing of the sensors, the strain was applied using a three-coordinate displacement table (TSA50-A, Zolix), while the output signals were collected using a desktop multimeter or a semiconductor device analyzer (8846A, Fluke; B1500A, Keysight).

3. RESULTS AND DISCUSSION

3.1. 2D-to-3D Morphology Transformation. Figure 1 illustrates the schematic of the fabricated a-C/PDMS strain sensor based on the concept of 2D-to-3D transformation. As shown in Figure 1a, a hardened layer is shown in the surface of a pristine PDMS substrate due to Ar ion bombardment. As shown in Figure 1b, due to the lasting energetic ion bombardment, a high intrinsic residual compressive stress was formed in the a-C films (assuming $\sigma_x = \sigma_y$), and a stress mismatch between a-C and PDMS appeared,[22] which was caused by the high sp^3 content[28] (Table S1 and Figure S2). Further increasing the thickness of a-C films easily stimulated the buckling of a-C films as a consequence of the relaxation of the compressive stress in the a-C layer without the film peeling off (Figure 1c). Thus, wrinkles were yielded followed by the formation of 3D electrical junctions through fractures in the a-C/PDMS system, as illustrated in Figure 1d. Then, the numerous 3D junctions played a key role in the a-C/PDMS stretchable strain sensor, which is shown in Figure 1e.

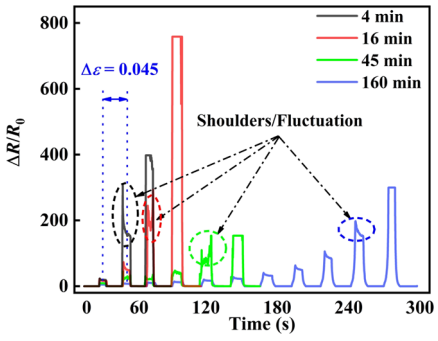

Figure 4. Variable strain test results of the 4, 16, 45, and 160 min samples, showing an obvious electrical difference between these samples (the strain increment is 0.045 between two adjacent peaks, and the flat head means beyond the sensitivity of the instrument).

To investigate the 2D-to-3D morphology transformation, we adjusted the thickness of the a-C film in the range of ~25 nm to 1 μm by simply controlling the deposition time. As shown in Figure 2(a1), the plasma etching process hardened the PDMS surface as expected. Random wrinkles appeared in the hardened layer. Upon a-C deposition, the release of almost 1.97 GPa (Table S2) compressive residual stress yielded wrinkles, valleys, or cracks in the multilayer structure, as shown in Figure 2(b–e). Assuming that the substrate after the Ar plasma treatment is an ideal plane on the scale of several micrometers, using Hooke's law, the strain caused by the a-C film in the 2D plane can be calculated as

$$\varepsilon_x = \frac{1}{E_{\mathrm{Com}}}(\sigma_x - \nu\sigma_y) \quad (1)$$

$$\varepsilon_y = \frac{1}{E_{\mathrm{Com}}}(\sigma_y - \nu\sigma_x) \quad (2)$$

where ε_x and ε_y are the strains along the x and y directions, respectively, E_{Com} and ν are the composite Young's modulus and Poisson's ratio of the multilayer structure (a-C/hardened PDMS/surface layer of the PDMS substrate), respectively, and σ_x and σ_y are the stresses caused by the a-C film along the x and y directions, respectively. We assumed $\sigma_x = \sigma_y$ as the deposition of the a-C film was uniform and stable, and thus $\varepsilon_x = \varepsilon_y$.

The Young's modulus of PDMS is only 0.57 MPa and that of the hardened PDMS is below 100 MPa,[29] while that of a-C is approximately 185.2 GPa (Table S3). The compressive residual stress of the a-C film was almost 1.97 GPa (Table S2). Thus, the release of the very large compressive stress along the x/y direction would cause obvious wrinkles[30] because the true surface was not an ideal 2D plane. As shown in Figure 2(b3), rod-like wrinkles along random directions appeared even in the only ~25 nm thick a-C film after 4 min of deposition. But the surface was still flat, which meant that the contact area between the scales was small and mainly dominated by the cross section of the film, as shown in Figure 2(b1), which was a typical 2D contact mode. Then, the thickness of the as-deposited a-C film increased at a rate of almost 6.25 nm/min. E_{Com} gradually approached $E_{\mathrm{a\text{-}C}}$, and the wrinkles did not change significantly. However, the high compressive stress should be still released through other mechanisms, such as through curved scales or even generated cracks. Compared with the thickness of the a-C film, obvious valleys are seen in Figure 2(c2, d2, and e2) with depths of almost 1.83 to 12.3 μm, which indicated that the contact area became much bigger than that in the 2D mode. In other words, 3D junctions appeared. The whole surface was then separated into numerous scales but not torn as shown in Figure 2(b1, c1, d1). With the increase of the deposition time up to 160 min, the thickness of the a-C film reached approximately 1 μm. The edges of the scales were severely curved, and then cracks appeared, as shown in Figure 2(e1 and e3). This important characteristic 2D-to-3D transformation might provide the sensor with unique electrical performances.

3.2. Strain Sensing Performance of the a-C/PDMS Stretchable Strain Sensor. Plastic deformation appeared in

https://dx.doi.org/10.1021/acsami.0c12073
ACS Appl. Mater. Interfaces 2020, 12, 45549–45557

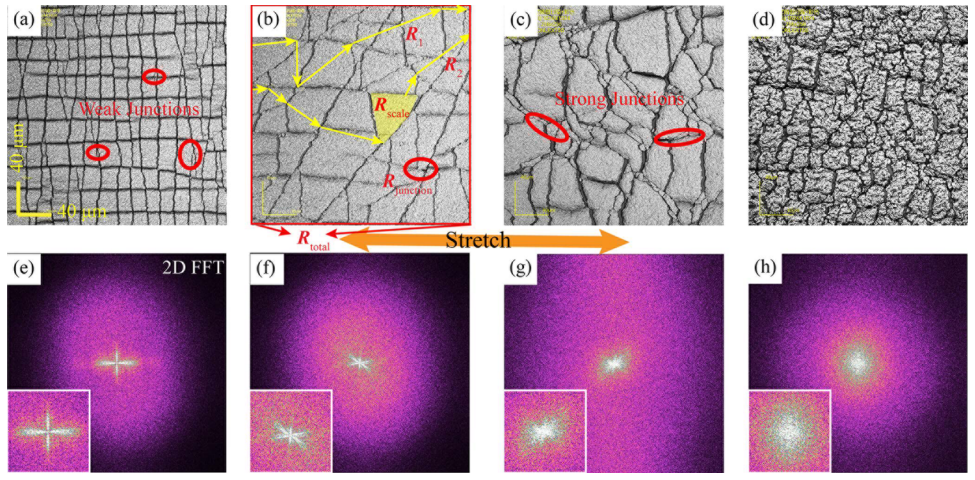

Figure 5. Analysis of the electrical conduction mechanism on a 2D level by confocal microscopy and 2D FFT. (a–d) Images of 4, 16, 45, and 160 min samples in which scales, cracks, junctions, and representative conductive paths are shown (under ε = 0.2), respectively. (e–h) 2D FFT results corresponding to the above images, showing the degree of order decreasing apparently.

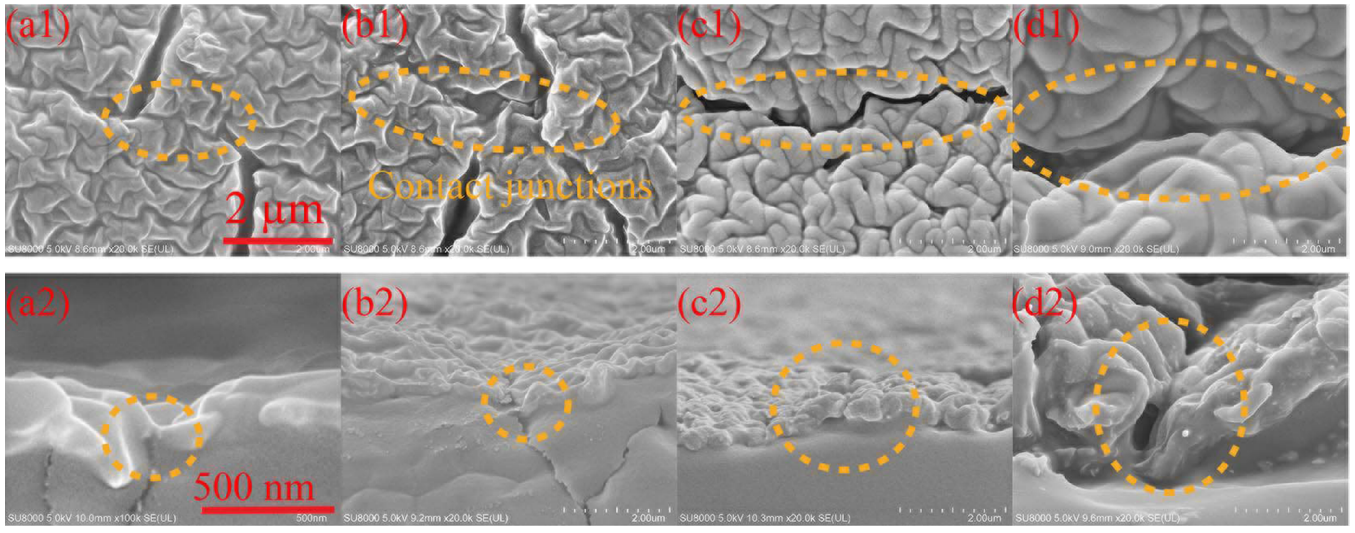

Figure 6. Analysis of the electrical conduction mechanism on a 3D level. (a–d) SEM images of the conductive junctions (top views in Series 1 and cross-sectional views in Series 2) of the 4, 16, 45, and 160 min samples, respectively, showing that the edge of the scale is bended by the a-C film and then the depth of the junction increases as the thickness increases.

the first cycle, which is shown in Figure S3, so the data for this work were recorded after it. Figure 3a shows the good stretchability of the sensor. The sample could easily measure a large strain of up to 0.5 and could be returned to the initial state well. Moreover, it exhibited satisfactory antioverload ability. Even for stretching up to 200%, the electrical performance and original shape were stable after the release to the original state, and the corresponding video is presented in real-time (Movie S1). Figure 3b presents the sensitivity test results for the a-C/PDMS sensor, that is, $\Delta R/R_0$ versus the strain. GF = $\Delta R/R_0/\varepsilon$ = $(R - R_0)/R_0/\varepsilon$, where R is the resistance under loading, R_0 is the original value (R_0 was about 3.2 MΩ in the following test), and ε is the strain. We show the results for the 160 min sample as a representative sample owing to its better performances. The maximum GF of the 160 min sample was 746.7 and the output signal curve is smooth, which is of advantage for practical applications. Considering that a linear signal is more convenient for understanding of the performance, we have divided the curve into three stages. In stage$_1$ (ε = 0–0.25), the slope of the fitted line is about 198.8, and R^2 (coefficient of determination) is equal to 0.992, which shows a good linear relation. In stage$_2$ (ε = 0.25–0.43), the slope of the fitted line is about 599.3, and R^2 = 0.986, which is also satisfied. Furthermore, in stage$_3$ (0.43–0.5), the slope is about 2684.9 while R^2 = 0.962, which shows the faint decrease in curve linearity.

To show the high-performance repeatability of the sensor under various loadings, we further present the test results for five cycles at strains of 0.25, 0.34, 0.42, and 0.48. Figure 3c shows the repeatability test results for 5000 cycles for the 160 min sample at a strain of 0.10. After a few stabilization cycles, the sample exhibited excellent repeatability. The waveform demonstrated good uniformity, as shown in the inset. Moreover, Figure 3d shows that the resistance signals had good stability and repeatability at each strain loading cycle. Most importantly, the sample exhibited a fast response with a response time below 50 ms, which implies that the a-C/PDMS sensor could sense rapidly changing signals, as shown in Figure 3e. On the other side, Figure 3f and g show that the temperature and time drifts at zero position were only 25 ppmFS·°C^{-1} in the range of −20 to 155 °C and 75 ppm FS during 1 h, respectively, which is

https://dx.doi.org/10.1021/acsami.0c12073
ACS Appl. Mater. Interfaces 2020, 12, 45549–45557

Table 1. Summary of Characteristics of Reported Crack-Based Piezoresistive Flexible Sensors (ITO: Indium Tin Oxide; PET: Polyethylene Terephthalate; RGO: Reduced Graphene Oxide; CNT: Carbon Nanotube; and TPU: Thermoplastic Polyurethanes)

no.	contact mode	GF	range (strain)	fabrication	ref.
1	2D	1058	0.0012	sputtering of a Au film on a PDMS substrate	12
2	2D	5888	0.02	sputtering of a Au film on PDMS cracks	11
3	2D	~ 20,000	0.01	sputtering of ITO on a PET substrate	13
4	3D	~ 9.4	~ 0.50	embedment of RGO/CNTs/PDMS into cellulose sponges	34
5	3D	155.7	2.00	embedment of RGO into a TPU 3D fiber mat	16
6	3D	178	0.30	graphene−PDMS 3D synthesis	3
7	3D	352	1.50	brushing of graphene and CNT ink	15
8	3D	1054	0.26	spraying of a graphene ink onto a PDMS substrate	10
this work	2D-to-3D	746.7	0.5	sputtering of an a-C film to fabricate 3D junctions	

advantageous for long-term applications under variable harsh environments. It could be said that the a-C/PDMS sensor would be a core component of a high-performance flexible strain-sensing device in future.

Notably, the samples exhibited considerably different electrical performances although only the thickness of a-C was changed, as shown in Figure 4. The GFs of the samples with thicker a-C films were very large. The resistances of the 4 and 16 min samples quickly increased over the measurement range (1200 MΩ) of the multimeter. In addition, the signals of these two samples sharply fluctuated during loading. This phenomenon was gradually suppressed with the increase in the a-C film thickness. When the a-C deposition time was increased to 45 min, the sensor sample could detect strain up to 0.30. When we increased the time to 160 min, the measurement range reached up to 0.50 and the fluctuation disappeared. Additionally, shoulders appeared in the signals in the beginning of each loading process, which might be attributed to the creep of the PDMS substrate.[31] In summary, the thickness of the a-C film determined the GF of the sensors, effective measurement range, and stability of the signal, which are valuable for property modulation. As the thickness could be well controlled by simply adjusting the deposition time, this method facilitates the development of a high-performance sensor with quite a facile strategy.

3.3. Electrical Conduction Mechanism of the a-C/PDMS Stretchable Strain Sensor. The high sensitivity of the a-C/PDMS sensor originates from the crack-based electrical conduction mechanism on a 2D level.[12,32] In this study, the piezoresistive performance was modulated by controlling the distribution of cracks and scales in-plane by varying the a-C film deposition time. As shown in Figure 4, the series of a-C films with different thicknesses exhibited different strains and thus various morphologies on the PDMS surface. At $\varepsilon = 0.2$, scales moved away from each other along the stretching direction and were compressed along the perpendicular direction owing to the Poisson effect.[33] Junctions connected the separated scales and formed conductive paths. Thus, their distribution and dimensions led to different piezoresistive performances. To elucidate the mechanism of the effect of the a-C thickness on the performance of the sensor, we carried out further analysis on the evolution of the microstructure in the a-C/PDMS system.

As shown in Figure 5, the change in thickness of the a-C film caused different 2D morphologies under strain. As shown in Figure 5a, a large number of regular cracks perpendicular to the strain direction were observed on the surface of the 4 min sample, which were detrimental as they severely broke the conductive loop, that is, caused an open circuit. In addition, a few weak junctions, small and unstable, still connected some scales. Owing to this electrical structure, the 4 min sample exhibited very large resistivity and GF. In the 16 min sample, as shown in Figure 5b, the cracks' orientation was more complex. Inclined cracks were observed and the junctions were stronger, which yielded a more stable conductive path (paths 1−n are marked as representative in this figure). The resistance of each conductive path (R_n) can be calculated by adding its resistances of scales and junctions (R_{scale} and $R_{junction}$). The total resistance of the sample (R_{total}) originates from several multiple conductive paths (R_1, R_2,..., R_n). Owing to more junctions and conductive paths, the 16 min sample had smaller resistivity under strain than that of the 4 min sample.

Figure 5c shows the morphology of the 45 min sample. The slant junctions between larger scales were stronger as they were longer. In addition, a large number of small scales emerged among the large scales due to the large residual stress of the ~300 nm thick a-C film. Thus, the conductive path was considerably more complex, and the resistivity continued to decrease. Figure 5d shows that the scales are smaller as the ~1 μm thick a-C film tore the substrate to release the very large compressive stress. In addition, many strong junctions were formed, which provided the largest measurement range and the most stable piezoresistive performance. As shown in Figure S4, using ImageJ, the number and area of the scales are counted. In general, a narrow distribution of the size and less quantity of the scales are deleterious for a comprehensive performance. However, the relation between the electrical performance and the counted result is not obvious enough.

Then, the two-dimensional fast Fourier transform (2D FFT) method was used to analyze Figure 5a−d, and the results are shown in Figure 5e−h. The 2D FFT images show an obvious disordering tendency from 4 min to 160 min samples. In particular, for the 160 min sample, the distribution of the scales and cracks was almost completely disordered, which means that more junctions and conductive paths will exist, under a certain strain, resulting in the decrease of resistance. In other words, disorder means a better comprehensive performance. Furthermore, the images reveal further details on a 3D level, which is beneficial to elucidate the origin of the differences in electrical conductivity and stability.

The SEM images shown in Figure 6 show further 3D details of the sensor samples. Figure 6a shows the detailed morphology of the conductive junction of the 4 min sample. Adjacent scales contacted as two flat tables, which had a small contact surface. This contact mode led to high resistivity and low stability. In the 16 min sample, as shown in Figure 6b, the scales began to bend and the contact area was larger, which caused a higher electrical conductivity performance. Figure 6c shows that the scales were considerably bent, and thus the 2D contact mode began to transfer into the 3D mode. The scales covered with the a-C film contacted with each other in large areas, which made this contact mode more stable. When the deposition time was increased to

https://dx.doi.org/10.1021/acsami.0c12073
ACS Appl. Mater. Interfaces 2020, 12, 45549−45557

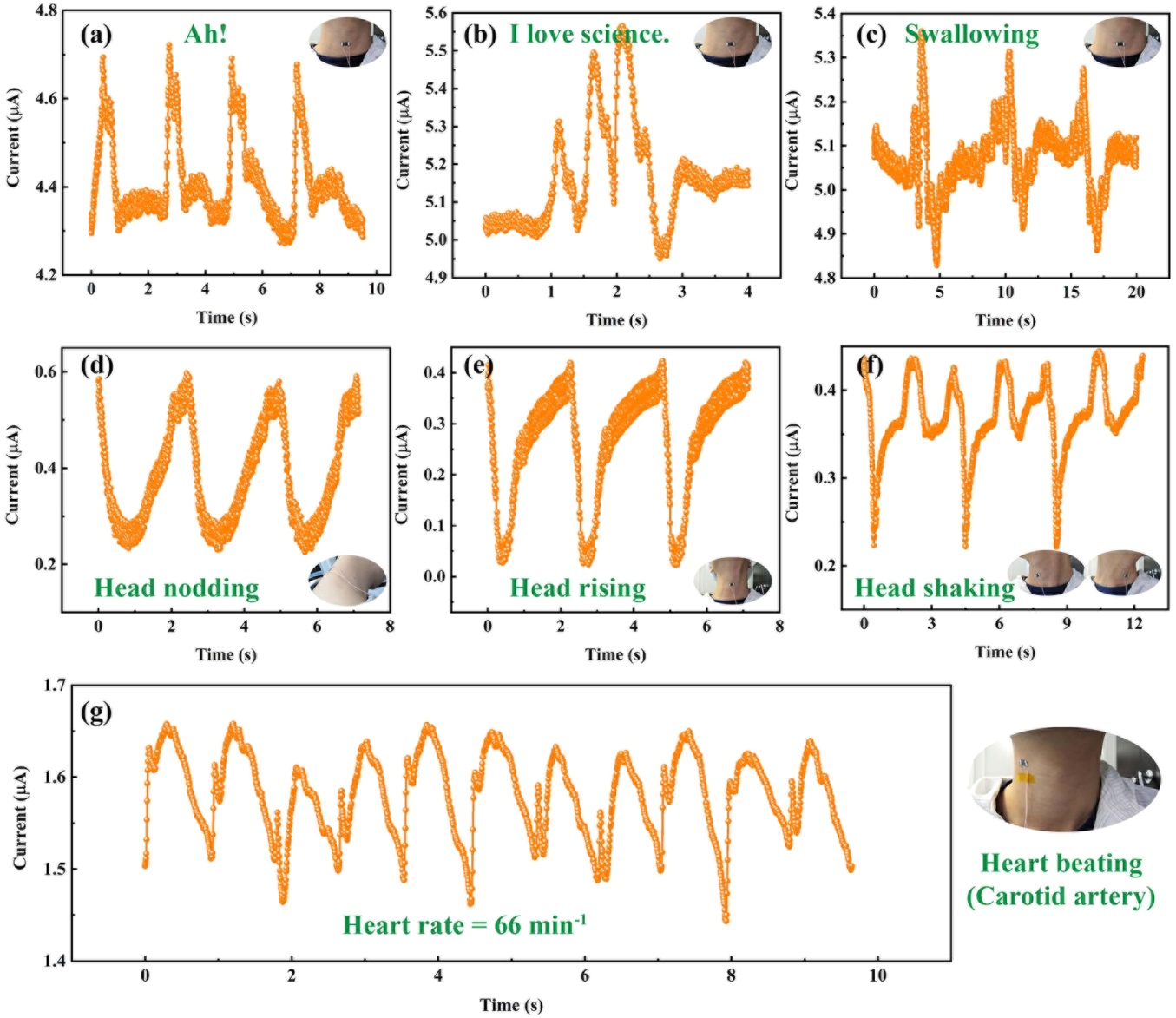

Figure 7. Monitoring of physiological signals of the human neck. In this test, a voltage of 3 V was applied to the sensor and the current signals were collected. Signals during (a, b) speaking ("Ah!" and "I love science"), (c) swallowing, (d–f) head nodding, rising, and shaking, and (g) heart beating. Each signal shows a unique waveform, which is beneficial to distinguish them. The inset in each figure shows the pasting position of the sensor.

160 min, as shown in Figure 6d, the scales were sharply bent at the edges because of the very large stress from the a-C film. Then, the wrinkles contacted with each other through the largest areas in all samples. In addition, the wrinkles were smoother when the thickness was increased, which yielded a higher contact performance (Figure S5). Additionally, the sheet resistance of the 160 min a-C film was smallest in all samples (Table S1) and its thickness was approximately 1 μm so that the resistivity of the scales had the smallest value among all samples. As a result, the 160 min sample exhibited the most stable contact and highest comprehensive piezoresistive performance.

In summary, using 2D a-C deposition, 3D contact junctions were first and easily fabricated owing to the very large residual compressive stress, which greatly improved the compression performance of the sensor. The simple 2D-to-3D transformation provided the sensor with a very large GF, a large measurement range, and satisfactory stability. As summarized in Table 1, related studies based on the 2D contact mode have demonstrated very large GFs in the range of ~1000 to 20,000. However, the measurement strain range was below 0.02, which is not beneficial for applications on flexible substrates. For the 3D mode, the measurement range was 0.30–2.00. However, most of the structures exhibited GFs of several hundreds or even below 10, which hinders their application in the measurement of small strain signals. In this study, using simple sputtered a-C films, usually used to fabricate 2D structures, the 2D contact mode of junctions was changed into the 3D mode, which provides an efficient and automated fabrication. Owing to the stability of the 3D junctions, we first reported that the a-C-based sensors exhibited a large measurement range up to almost 0.5, while the GF was up to 746.7, which combines the advantages of the 2D and 3D structures.

3.4. Monitoring of Human Physiological Signals of the Neck Using the Sensor. The very large GF and satisfactory flexibility make the sensor promising for the monitoring of weak strain signals on curved surfaces, for example, on the human

https://dx.doi.org/10.1021/acsami.0c12073
ACS Appl. Mater. Interfaces 2020, 12, 45549–45557

neck. The human neck has various physiological functions, for example, in speaking, head nodding, rising, and shaking, and heart beating. The real-time monitoring of these signals is valuable for speech recognition and prevention of cervical vertebra and heart-related diseases. In this study, as shown in Figure 7a and b, the sensor could distinguish words when it was pasted on the position of the vocal cords, and sentences could also be recognized. Moreover, the swallowing signal could be easily recognized in this position as it has a specific feature advantageous for signal extraction, as shown in Figure 7c. The movement of the neck could also be monitored using the sensor. Head nodding, rising, and shaking were distinguished through their significant signals, as shown in Figure 7d–f, and the corresponding video of the head rising test is presented in real-time (Movie S2). The shaking direction could be obtained by pasting the sensor slightly away from the center line of the neck. Even the heart health with tiny pressure changes could be monitored by pasting the sensor at the position of the carotid artery. As illustrated in Figure 7g, the heart-beating signal of a healthy calm male was shown with excellent repeatability, where the heart rate was approximately 66 min^{-1}. Furthermore, the device can also sensitively monitor other physiological signals involving strain changes, such as breathing, facial expressions, and body movements.

4. CONCLUSIONS

A simple 2D-to-3D electrical junction transformation strategy based on amorphous carbon films was first proposed, originating from the release of the very high residual compressive stress and large differences in Young's modulus of the a-C/hardened PDMS/PDMS multilayer system. Using this method, cracks and 3D contact junctions were introduced and controlled successfully in the sensor, which provided both very high sensitivity and a large measurement range. Its maximum GF was 746.7, while the measurement strain range was up to 0.5. In addition, the one-step method was efficient and economical as only traditional DC sputtering was used to obtain the 2D-to-3D transformation by adjusting the thickness of the a-C film, without the use of an auxiliary prestretching device or extra-heating in the one-step process. The fabricated sensor exhibited good repeatability during the 5000 cycles. The combined time and temperature drift performances were also quite satisfactory compared to other reported results in the literature. The monitoring of human motions and physiological signals of the neck during speaking, swallowing, head nodding, rising, and shaking, and heart beating showed the excellent performance of the sensor in real applications.

■ ASSOCIATED CONTENT

Supporting Information

The Supporting Information is available free of charge at https://pubs.acs.org/doi/10.1021/acsami.0c12073.

Phase content and sheet resistance of the a-C films; residual stress test result of the a-C films; Young's modulus and hardness test result of the a-C films; schematic of DC sputtering for a-C deposition; XPS C1s spectra of the a-C films; three-cycle load–strain curve of the 160 min sample; count result of the area and number of the scales; and AFM-measured morphology of a-C SSES and the height information (PDF)

Antioverload test of the sensor (MP4)

Response of the sensor to head rising (MP4)

■ AUTHOR INFORMATION

Corresponding Authors

Qi Zhang – *State Key Laboratory for Mechanical Manufacturing Systems, School of Mechanical Engineering, Xi'an Jiaotong University, Xi'an 710049, China;* orcid.org/0000-0003-2152-3313; Email: zhq0919@xjtu.edu.cn

Peng Guo – *Key Laboratory of Marine Materials and Related Technologies, Zhejiang Key Laboratory of Marine Materials and Protective Technologies, Ningbo Institute of Materials Technology and Engineering, Chinese Academy of Sciences, Ningbo 315201, China*; Email: guopeng@nimte.ac.cn

Yulong Zhao – *State Key Laboratory for Mechanical Manufacturing Systems, School of Mechanical Engineering, Xi'an Jiaotong University, Xi'an 710049, China*; Email: zhaoyulong@xjtu.edu.cn

Aiying Wang – *Key Laboratory of Marine Materials and Related Technologies, Zhejiang Key Laboratory of Marine Materials and Protective Technologies, Ningbo Institute of Materials Technology and Engineering, Chinese Academy of Sciences, Ningbo 315201, China; Center of Materials Science and Optoelectronics Engineering, University of Chinese Academy of Science, Beijing 100049, China;* orcid.org/0000-0003-2938-5437; Email: aywang@nimte.ac.cn

Authors

Xin Ma – *State Key Laboratory for Mechanical Manufacturing Systems, School of Mechanical Engineering, Xi'an Jiaotong University, Xi'an 710049, China; Key Laboratory of Marine Materials and Related Technologies, Zhejiang Key Laboratory of Marine Materials and Protective Technologies, Ningbo Institute of Materials Technology and Engineering, Chinese Academy of Sciences, Ningbo 315201, China*

Xiaoshan Tong – *State Key Laboratory for Mechanical Manufacturing Systems, School of Mechanical Engineering, Xi'an Jiaotong University, Xi'an 710049, China*

Complete contact information is available at: https://pubs.acs.org/10.1021/acsami.0c12073

Notes

The authors declare no competing financial interest.

■ ACKNOWLEDGMENTS

This research was supported by the National Natural Science Foundation of China (51805425), the K.C.Wong Education Foundation (GJTD-2019-13), the National Natural Science Foundation of Shaanxi Province (2018JQ5018), the Ningbo Science and Technology Innovation Project (2018B10012), and the Fundamental Research Funds for the Central Universities (xzy022019038 and xjj2018046).

■ REFERENCES

(1) Kenry; Yeo, J. C.; Lim, C. T. Emerging Flexible and Wearable Physical Sensing Platforms for Healthcare and Biomedical Applications. *Microsyst. Nanoeng.* **2016**, *2*, 16043.

(2) Ma, Y.; Liu, N.; Li, L.; Hu, X.; Zou, Z.; Wang, J.; Luo, S.; Gao, Y. A Highly Flexible and Sensitive Piezoresistive Sensor Based on Mxene with Greatly Changed Interlayer Distances. *Nat. Commun.* **2017**, *8*, 1207.

(3) Patole, S. P.; Reddy, S. K.; Schiffer, A.; Askar, K.; Prusty, B. G.; Kumar, S. Piezoresistive and Mechanical Characteristics of Graphene Foam Nanocomposites. *ACS Appl. Nano Mater.* **2019**, *2*, 1402–1411.

(4) Stassi, S.; Cauda, V.; Canavese, G.; Pirri, C. F. Flexible Tactile Sensing Based on Piezoresistive Composites: A Review. *Sensors (Basel)* **2014**, *14*, 5296−5332.
(5) Chortos, A.; Liu, J.; Bao, Z. Pursuing Prosthetic Electronic Skin. *Nat. Mater.* **2016**, *15*, 937−950.
(6) Zhu, S.-E.; Krishna Ghatkesar, M.; Zhang, C.; Janssen, G. C. A. M. Graphene Based Piezoresistive Pressure Sensor. *Appl. Phys. Lett.* **2013**, *102*, 161904.
(7) Yoshikawa, G.; Akiyama, T.; Gautsch, S.; Vettiger, P.; Rohrer, H. Nanomechanical Membrane-Type Surface Stress Sensor. *Nano Lett.* **2011**, *11*, 1044−1048.
(8) Li, Y. X.; He, T. Y.; Shi, L. J.; Wang, R. R.; Sun, J. Strain Sensor with Both a Wide Sensing Range and High Sensitivity Based on Braided Graphene Belts. *ACS Appl. Mater. Interfaces* **2020**, *12*, 17691−17698.
(9) Song, H.; Zhang, J.; Chen, D.; Wang, K.; Niu, S.; Han, Z.; Ren, L. Superfast and High-Sensitivity Printable Strain Sensors with Bio-inspired Micron-Scale Cracks. *Nanoscale* **2017**, *9*, 1166−1173.
(10) Yang, Y. F.; Tao, L. Q.; Pang, Y.; Tian, H.; Ju, Z. Y.; Wu, X. M.; Yang, Y.; Ren, T. L. An Ultrasensitive Strain Sensor with a Wide Strain Range Based on Graphene Armour Scales. *Nanoscale* **2018**, *10*, 11524−11530.
(11) Han, Z.; Liu, L.; Zhang, J.; Han, Q.; Wang, K.; Song, H.; Wang, Z.; Jiao, Z.; Niu, S.; Ren, L. High-Performance Flexible Strain Sensor with Bio-Inspired Crack Arrays. *Nanoscale* **2018**, *10*, 15178−15186.
(12) Liu, X.; Zhu, Y.; Nomani, M. W.; Wen, X.; Hsia, T.-Y.; Koley, G. A Highly Sensitive Pressure Sensor Using a Au-Patterned Polydimethylsiloxane Membrane for Biosensing Applications. *J. Micromech. Microeng.* **2013**, *23*, No. 025022.
(13) Cairns, D. R.; Witte, R. P.; Sparacin, D. K.; Sachsman, S. M.; Paine, D. C.; Crawford, G. P.; Newton, R. R. Strain-Dependent Electrical Resistance of Tin-Doped Indium Oxide on Polymer Substrates. *Appl. Phys. Lett.* **2000**, *76*, 1425−1427.
(14) Shi, J.; Bin, S.; Li, H.; Xia, K.; Zhang, X.; Ding, G.; Pan, T.; Yang, Z. A Flexible Pressure Sensor by Induced Ordered Nano Cracks Filled with Multilayer Graphene Oxide Composite Film as a Conductive Fine-Wire Network for Higher Sensitivity. *Flex. Print. Electron.* **2019**, *4*, No. 015003.
(15) Tang, W.; Yan, T.; Wang, F.; Yang, J.; Wu, J.; Wang, J.; Yue, T.; Li, Z. Rapid Fabrication of Wearable Carbon Nanotube/Graphite Strain Sensor for Real-Time Monitoring of Plant Growth. *Carbon* **2019**, *147*, 295−302.
(16) Wang, Y.; Hao, J.; Huang, Z.; Zheng, G.; Dai, K.; Liu, C.; Shen, C. Flexible Electrically Resistive-Type Strain Sensors Based on Reduced Graphene Oxide-Decorated Electrospun Polymer Fibrous Mats for Human Motion Monitoring. *Carbon* **2018**, *126*, 360−371.
(17) Zhong, Y.; Tan, X.; Shi, T.; Huang, Y.; Cheng, S.; Chen, C.; Liao, G.; Tang, Z. Tunable Wrinkled Graphene Foams for Highly Reliable Piezoresistive Sensor. *Sens. Actuator A-Phys.* **2018**, *281*, 141−149.
(18) Al-Rashed, R.; Lopez Jimenez, F.; Marthelot, J.; Reis, P. M. Buckling Patterns in Biaxially Pre-Stretched Bilayer Shells: Wrinkles, Creases, Folds and Fracture-Like Ridges. *Soft Matter* **2017**, *13*, 7969−7978.
(19) Yuan, H.; Wu, K.; Zhang, J.; Wang, Y.; Liu, G.; Sun, J. Curvature-Controlled Wrinkling Surfaces for Friction. *Adv. Mater.* **2019**, *31*, 1900933.
(20) Liu, Y.; Wang, X.; Xu, Y.; Xue, Z.; Zhang, Y.; Ning, X.; Cheng, X.; Xue, Y.; Lu, D.; Zhang, Q.; Zhang, F.; Liu, J.; Guo, X.; Hwang, K. C.; Huang, Y.; Rogers, J. A.; Zhang, Y. Harnessing the Interface Mechanics of Hard Films and Soft Substrates for 3d Assembly by Controlled Buckling. *Proc. Natl. Acad. Sci. U. S. A.* **2019**, *116*, 15368−15377.
(21) Meng, L.; Li, Y.; Liu, T. S.; Zhu, C.; Li, Q. Y.; Chen, X.; Zhang, S.; Zhang, X.; Bao, L.; Huang, Y.; Xu, F.; Ruoff, R. S. Wrinkle Networks in Exfoliated Multilayer Graphene and Other Layered Materials. *Carbon* **2020**, *156*, 24−30.
(22) Ahmed, S. F.; Rho, G.-H.; Lee, K.-R.; Vaziri, A.; Moon, M.-W. High Aspect Ratio Wrinkles on a Soft Polymer. *Soft Matter* **2010**, *6*, 5709−5714.
(23) Guo, P.; Li, X.; Sun, L.; Chen, R.; Ke, P.; Wang, A. Stress Reduction Mechanism of Diamond-Like Carbon Films Incorporated with Different Cu Contents. *Thin Solid Films* **2017**, *640*, 45−51.
(24) Sheeja, D.; Tay, B. K.; Sze, J. Y.; Yu, L. J.; Lau, S. P. A Comparative Study between Pure and Al-Containing Amorphous Carbon Films Prepared by Fcva Technique Together with High Substrate Pulse Biasing. *Diamond Relat. Mater.* **2003**, *12*, 2032−2036.
(25) Ma, X.; Guo, P.; Tong, X.; Zhao, Y.; Zhang, Q.; Ke, P.; Wang, A. Piezoresistive Behavior of Amorphous Carbon Films for High Performance Mems Force Sensors. *Appl. Phys. Lett.* **2019**, *114*, 253502.
(26) Ma, X.; Tong, X.; Guo, P.; Zhao, Y.; Zhang, Q.; Li, H.; Chen, R.; Wang, A. Mems Piezo-Resistive Force Sensor Based on Dc Sputtering Deposited Amorphous Carbon Films. *Sens. Actuator A-Phys.* **2020**, *303*, 111700.
(27) Lee, S.; Byeon, E.; Jung, S.; Kim, D. G. Heterogeneity of Hard Skin Layer in Wrinkled Pdms Surface Fabricated by Ar Ion-Beam Irradiation. *Sci. Rep.* **2018**, *8*, 14063.
(28) Shen, Y.; Ou, Y.; Wang, H.; Liao, B.; Wu, X.; Zhang, X. Wear and Corrosion Resistance of Diamond-Like Carbon Coatings Deposited by Filtered Cathodic Vacuum Arc Coupled with a High-Voltage Pulse Power. *Mater. Res. Express* **2019**, *6*, 105625.
(29) Glatz, B. A.; Tebbe, M.; Kaoui, B.; Aichele, R.; Kuttner, C.; Schedl, A. E.; Schmidt, H. W.; Zimmermann, W.; Fery, A. Hierarchical Line-Defect Patterns in Wrinkled Surfaces. *Soft Matter* **2015**, *11*, 3332−3339.
(30) Kim, S. J.; Yoon, J.-I.; Moon, M.-W.; Lee, K.-R. Frictional Behavior on Wrinkle Patterns of Diamond-Like Carbon Films on Soft Polymer. *Diamond Relat. Mater.* **2012**, *23*, 61−65.
(31) Charitidis, C. A.; Koumoulos, E. P.; Tsikourkitoudi, V. P.; Dragatogiannis, D. A.; Lolas, G. Influence of Accelerated Aging on Nanomechanical Properties, Creep Behaviour and Adhesive Forces of Pdms. *Plast. Rubber Compos.* **2013**, *41*, 94−99.
(32) Noh, J.-S. Cracked Titanium Film on an Elastomeric Substrate for Highly Flexible, Transparent, and Low-Power Strain Sensors. *Nanoscale Res. Lett.* **2013**, *8*, 441.
(33) Graz, I. M.; Cotton, D. P. J.; Lacour, S. P. Extended Cyclic Uniaxial Loading of Stretchable Gold Thin-Films on Elastomeric Substrates. *Appl. Phys. Lett.* **2009**, *94*, No. 071902.
(34) Wu, S.; Peng, S.; Wang, C. H. Stretchable Strain Sensors Based on Pdms Composites with Cellulose Sponges Containing One- and Two-Dimensional Nanocarbons. *Sens. Actuator A-Phys.* **2018**, *279*, 90−100.

https://dx.doi.org/10.1021/acsami.0c12073
ACS Appl. Mater. Interfaces 2020, 12, 45549−45557